



Earth and Space Science



RESEARCH ARTICLE

10.1029/2019EA000701

Key Points:

- Diurnal variations of tropospheric delay and weighted mean temperature are investigated with ERA5 hourly data
- A new model that can estimate tropospheric delay and weighted mean temperature over China with higher spatiotemporal resolutions is built
- This new model is validated and compared with the canonical GPT2w model

Supporting Information:

- Supporting Information S1

Correspondence to:

B. Zhang,
sgzgb@whu.edu.cn

Citation:

Sun, Z., Zhang, B., & Yao, Y. (2019). An ERA5-based model for estimating tropospheric delay and weighted mean temperature over China with improved spatiotemporal resolutions. *Earth and Space Science*, 6, 1926–1941. <https://doi.org/10.1029/2019EA000701>

Received 6 MAY 2019

Accepted 11 SEP 2019

Accepted article online 21 OCT 2019

Published online 23 OCT 2019

Corrected 30 DEC 2019

This article was corrected on 30 DEC 2019. See the end of the full text for details.

©2019. The Authors.

This is an open access article under the terms of the Creative Commons Attribution-NonCommercial-NoDerivs License, which permits use and distribution in any medium, provided the original work is properly cited, the use is non-commercial and no modifications or adaptations are made.

An ERA5-Based Model for Estimating Tropospheric Delay and Weighted Mean Temperature Over China With Improved Spatiotemporal Resolutions

Zhangyu Sun¹, Bao Zhang¹ , and Yibin Yao¹

¹School of Geodesy and Geomatics, Wuhan University, Wuhan, China

Abstract Tropospheric delay is an important error source in Global Navigation Satellite System (GNSS) positioning and can also be used in water vapor monitoring. Many models have been built to correct tropospheric delays or to convert zenith wet delays to precipitable water vapor. However, these models suffer from limited resolutions (spatial resolution lower than 1° and temporal resolution lower than 6 hr), which affects their performance. The release of European Centre for Medium-Range Weather Forecasts ReAnalysis 5 (ERA5) provides the opportunity to lift this limit. In this study, we use the ERA5 hourly 0.5° × 0.5° data to build a new model over China, which integrates tropospheric delay correction for GNSS positioning and weighted mean temperature calculation for GNSS meteorology. By modeling the diurnal variations of zenith hydrostatic delay, zenith wet delay, and weighted mean temperature and the seasonal variations in their lapse rates, this model has the state-of-the-art spatial resolution of 0.5° × 0.5° and temporal resolution of 1 hr. We validate this new model by the ERA5 data, the radiosonde data, and the GNSS data in comparison with the canonical GPT2w model. The results show that the new model has better accuracies in terms of root-mean-square than the GPT2w model in all parameters. Especially, the new model well captures the diurnal variations in tropospheric delay and weighted mean temperature. This new model provides accurate tropospheric delays and weighted mean temperature simultaneously, which enables GNSS receivers to measure precipitable water vapor directly and also benefits GNSS positioning.

1. Introduction

When Global Navigation Satellite System (GNSS) signals travel through the neutral atmosphere, they undergo bending and time delay due to atmospheric refractivity. The bending effect is very small when the elevation angle is larger than 10° and thus usually neglected (Leick et al., 2015). The time delay-induced excess raypath measurement is called the tropospheric delay in the GNSS community.

The tropospheric delay is an important error source in GNSS positioning that should be well modeled and corrected. Tregoning and Herring (2006) pointed out that good a priori tropospheric delay information can improve the estimates of the coordinate and tropospheric delay parameters in GNSS positioning. The tropospheric delay can be divided into a hydrostatic delay caused by atmospheric gases in hydrostatic equilibrium and a wet delay primarily caused by water vapor (Askne & Nordius, 1987; Davis et al., 1985; Ifadis, 1993). Each component is usually considered as the product of the delay experienced at the zenith and the corresponding mapping functions (Davis et al., 1985). Traditional models, such as the Saastamoinen model (Saastamoinen, 1972) and the Hopfield model (Hopfield, 1971), require in situ meteorological observations to ensure their highest performances, but most GNSS stations are not equipped with meteorological sensors. Therefore, numerical weather prediction (NWP) products or empirical models are needed.

Though the data from the NWP models are better than those from the empirical models, they are not so easy for the GNSS community to access and use. For postprocessing, the GNSS users may afford time and devices to download the data from the Internet and do the data processing locally, but it is much more inconvenient than using empirical models. Given the slight improvement of using NWP products to using empirical models, the GNSS community tend to use the empirical models. For real-time applications, using the NWP products is even more difficult. So it is ideal to use the NWP products, but in practice for convenience's sake there is still demand for empirical models, especially for regions like China.

Hitherto, scientists have built many empirical models, which are roughly divided into two types. The first type is based on the meteorological parameters, such as the UNB models (Collins & Langley, 1997, 1998),

the EGNOS model (Dodson et al., 1999; Penna et al., 2001), the TropGrid models (Krueger et al., 2005; Schüller, 2014), the GPT models (Böhm et al., 2007, 2015; Lagler et al., 2013; Landskron & Böhm, 2018), and the ITG model (Yao et al., 2015). This type of models usually employs a table to represent empirical meteorological parameters and uses the Saastamoinen model or similar models to calculate tropospheric delays. The second type directly models the tropospheric delay, such as the GZTD models (Yao et al., 2016) and the IGGtrop models (Li et al., 2012, 2015, 2018). This type of models provides empirical tropospheric delay free of meteorological parameters.

The tropospheric delay contains important information about the neutral atmosphere. The zenith wet delay (ZWD) can be used to measure water vapor in the atmosphere. Davis et al. (1985) introduced the concept of weighted mean temperature (T_m). Askne and Nordius (1987) derived the approximate relationship between ZWD and precipitable water vapor (PWV), in which T_m is the critical parameter for converting ZWD to PWV. But the precise calculation of T_m depends on the vertical profile of temperature and water vapor pressure, which greatly limits the application of GNSS in monitoring water vapor. Bevis et al. (1992) found the linear relationship between T_m and surface temperature (T_s) and updated this relationship in 1994 (Bevis et al., 1994), which made the calculation of T_m very easy. The above work founded the base for operationally using GNSS to measure PWV. Since then, many scientists have proposed new methods to improve the calculation of T_m . Yao et al. (2012) proposed the Global Weighted Mean Temperature model which provides accurate empirical T_m worldwide and was updated and perfected in 2013 and 2014 (Yao et al., 2013, 2014). Other similar models are also established, including Chen et al. (2014), He et al. (2017), Zhang et al. (2017), Ding (2018), Yao et al. (2018), and Huang et al. (2018). In addition, some tropospheric delay models, such as the GPT2w model (Böhm et al., 2015), the TropGrid2 model (Schüller, 2014), and the ITG model (Yao et al., 2015), also provide empirical T_m .

Recently, Landskron and Böhm (2018) built the GPT3 model. Compared with its predecessor GPT2w, this model only updated the empirical mapping function coefficients. The zenith tropospheric delay and the T_m modules are unchanged. Balidakis et al. (2018) constructed the empirical model GFZ-PT. This model can additionally provide estimations of tropospheric gradients.

However, both the tropospheric delay models and the T_m models are largely based on data from NWP products. The previous NWP data have the highest temporal resolution of only 6 hr, which is insufficient to accurately reveal the phase and amplitudes of the diurnal and subdiurnal variations in tropospheric delay and T_m . Besides, their highest spatial resolution is only ~80 km. This low spatial resolution also brings uncertainties in estimating tropospheric delays and T_m .

The release of the European Centre for Medium-Range Weather Forecasts (ECMWF) ReAnalysis 5 (ERA5) hourly data provides the opportunity to build a sophisticated model incorporating tropospheric delay correction and T_m calculation with better accuracy and resolution. In this study, the ERA5 hourly data are used to investigate daily variations of zenith hydrostatic delay (ZHD), ZWD, and T_m . Then, they are used to construct a sophisticated model for tropospheric delay correction and T_m calculation. Through this work, we hope that the new model could better serve the GNSS meteorology and positioning than other models.

In this paper, we first describe the data used for modeling and validation (section 2). And then we illustrate how we model the ZHD, ZWD, and T_m (section 3). After the methodology, we validate the new model and present the model's accuracy information (section 4). Finally, we discuss the results and summarize the conclusions of this work (section 5).

2. Data

2.1. ECMWF ERA5 Reanalysis Data

ERA5 is the fifth generation ECMWF a T_m ospheric reanalysis of the global climate (Hersbach & Dee, 2016). Compared with previous ECMWF ERA-Interim reanalysis, the ERA5 reanalysis has improved the spatial resolution from ~80 to ~31 km and the temporal resolution from 6 to 1 hr (Albergel et al., 2018). In this study, the ERA5 hourly geopotential, temperature, and specific humidity data on 37 pressure levels are used. The geopotential data are used to calculate geopotential heights, which are then converted to WGS84 ellipsoid heights. The specific humidity data are used to calculate water vapor pressure (Böhm et al., 2015). Then the pressure, temperature, and water vapor pressure on the 37 pressure levels are used to calculate

tropospheric parameters including ZHD, ZWD, and T_m . Since the Saastamoinen model (Saastamoinen, 1972) can estimate ZHD with millimeter-level accuracy, we use this model to directly compute ZHD (mm) with the ERA5 pressure data:

$$ZHD = \frac{2.2768P}{1 - 0.00266\cos(2\varphi) - 0.00028h} \quad (1)$$

where P denotes the pressure (hPa), φ is the latitude (radian), and h is the height (km). ZWD (mm) and T_m (K) are calculated by the following equations (Bevis et al., 1992; Davis et al., 1985):

$$ZWD = 10^{-6} \int_h^{\infty} N_w dh \quad (2)$$

$$N_w = k'_2 \frac{e}{T} + k_3 \frac{e}{T^2} \quad (3)$$

$$T_m = \frac{\int_h^{\infty} \frac{e}{T} dh}{\int_h^{\infty} \frac{e}{T^2} dh} \quad (4)$$

where N_w denotes the wet refractivity, e and T indicate the water vapor pressure (hPa) and the temperature (K), and k'_2 and k_3 are the a T_m ospheric refractive index constants whose values are 22.97 K/hPa and 375463 K²/hPa (Rüeger, 2002). We use the ERA5 data from 2011 to 2018 with a temporal resolution of 1 hr to calculate ZHD, ZWD, and T_m for modeling and validation (the data from 2011 to 2017 are used for modeling, and the data in 2018 are used for validation).

2.2. Radiosonde Data

As important and accurate meteorological observations, the radiosonde data are usually used to evaluate other observations or model output, especially for the validation of T_m whose accurate determination requires vertical profiles of water vapor pressure and temperature. The radiosonde data used in this study are from Integrated Global Radiosonde Archive, which provides high-quality sounding observations from more than 1,500 radiosondes and sounding balloons worldwide since 1960s. The radiosonde usually launches twice daily at 00:00 and 12:00 UTC and provides meteorological profiles including pressure, temperature, and relative humidity on certain pressure levels. The water vapor pressure can be derived from the relative humidity (Wang et al., 2016). We use the radiosonde data in 2017 with a temporal resolution of 12 hr to calculate the ZHD, ZWD, and T_m by using the same method as illustrated in section 2.1, which are then used for validation.

2.3. GNSS Data

The International GNSS Service (IGS) archives and distributes zenith total delay (ZTD) estimates from the GNSS observation data at all IGS stations with a temporal resolution of 5 min and with a latency of about 4 weeks (Hackman & Byram, 2012). The accuracy of the ZTD estimates is specified with 4 mm by the IGS Central Bureau. The ZTD is a sum of ZHD and ZWD. We obtain GNSS-derived ZTD in 2018 with a temporal resolution of 5 min from the IGS archive and use these data to validate the tropospheric delay outputs from the new model.

3. Methods

3.1. Diurnal Variations of Tropospheric Delay and T_m

We perform a fast Fourier transform (FFT) analysis on the computed hourly ZHD, ZWD, and T_m , respectively, to investigate their diurnal variations. Since we focus on the diurnal and semidiurnal signals, we first use a high-pass filter to remove the low-frequency signals (whose periods are larger than 10 days). Then, we apply FFT analysis to the filtered ZHD, ZWD, and T_m to investigate their daily variations. Figure 1 shows the exemplary power spectrums at 15° north latitude and 100° east longitude (simply labeled as 15°N and 100° E hereafter).

The power spectrum of ZHD (Figure 1a) has two strong peaks at 1 and 0.5 days. Especially, the semidiurnal variation is even stronger than the diurnal variation by showing a greater peak at 0.5 day than at 1 day. These are caused by a T_m ospheric tides but have not been well modeled by tropospheric delay models so far due to

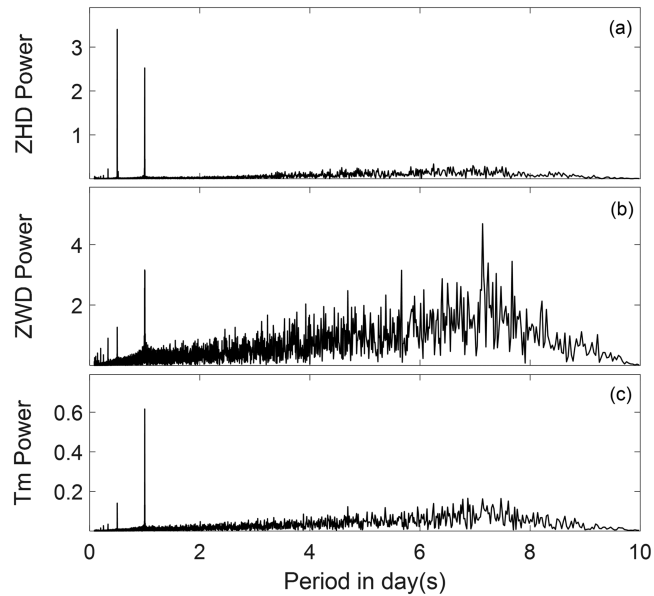


Figure 1. Power spectrums of (a) ZHD, (b) ZWD, and (c) T_m . Data for this example are from ERA5 grid data from 2011 to 2017 at 15°N and 100°E. ZHD = zenith hydrostatic delay; ZWD = zenith wet delay.

the limit in data temporal resolution. The power spectrum of ZWD (Figure 1b) shows a strong peak at 1 day. Nevertheless, it also shows other peaks, but these peaks have unclear meanings. They change with time and location and do not behave as regularly as the diurnal variations. The power spectrum of T_m (Figure 1c) shows a strong peak at 1 day and a weak peak at 0.5 day.

Based on the above spectral characteristics, we propose to use equation (5) to describe the diurnal and semi-diurnal variations of ZHD, ZWD, and T_m .

$$r(HOD) = A_0 + A_1 \cos\left(\frac{HOD}{24} 2\pi\right) + B_1 \sin\left(\frac{HOD}{24} 2\pi\right) + A_2 \cos\left(\frac{HOD}{24} 4\pi\right) + B_2 \sin\left(\frac{HOD}{24} 4\pi\right) \quad (5)$$

where $r(t)$ could be ZHD, ZWD, or T_m ; HOD indicates hour of day; and A_0 , A_1 , A_2 , B_1 , and B_2 are model coefficients.

However, these diurnal variations may not be revealed by ERA-Interim or other model data since their temporal resolutions are low. To demonstrate this, we resample the ERA5 hourly data (labeled as ERA5_1h hereafter) at 00:00, 6:00, 12:00, and 18:00 UTC to represent the ERA-Interim data (labeled as ERA5_6h hereafter). Then, the equation (5) is used to fit the ERA5_1h and the ERA5_6h data, respectively. The exemplary fitting results at grid point 15°N and 100°E on days of year (DOYs) 156–160, 2017 are given in Figure 2.

Figure 2a shows that the ZHD has apparently double-peak daily variations, but this is not revealed by the ERA5_6h data. The black curve (fit to ERA5_1h) well captures the double-peak variations, while the red curve (fit to ERA5_6h) fails, indicating that the ERA5_1h data are sufficient to solve equation (5) while the ERA5_6h data are not. Figure 2b shows that the ZWD has no regular diurnal variations, which should be due to the highly dynamic nature of water vapor. This leads to the poor modeling of ZWD no matter the ERA5_1h data or the ERA5_6h data are used. In Figure 2c, the T_m from the ERA5_1h data show a strong daily variation, which is consistent with the FFT results. This daily variation is also revealed by the ERA5_6h data. The black and red curves are close, indicating that both the ERA5_1h and the ERA5_6h data can determine equation (5).

3.2. Height Corrections for Tropospheric Delay and T_m

Height correction is an important aspect in establishing tropospheric delay and T_m models. If not properly accounted for, it will bring considerable uncertainties in modeling these parameters. Tropospheric delay models, such as the TropGrid model (Krueger et al., 2005) and the GPT2w model (Böhm et al., 2015),

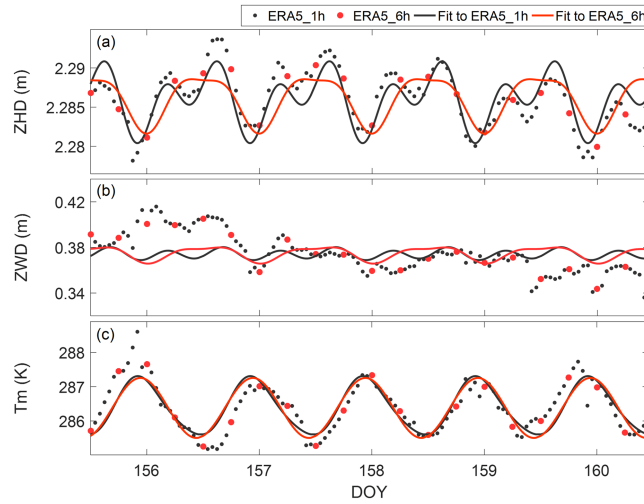


Figure 2. Variations of (a) ZHD, (b) ZWD, and (c) T_m at 15°N and 100°E on day of year 156–160, 2017. The fit to ERA5_1h data is labeled as “Fit to ERA5_1h,” and the fit to ERA5_6h data is labeled as “Fit to ERA5_6h.” ZHD = zenith hydrostatic delay; ZWD = zenith wet delay.

employ a physics-based approach to do the height correction, while the TropGrid2 model (Schüler, 2014) and the ITG model (Yao et al., 2015) employ an empirical exponential function. The former uses meteorological parameters to do the correction. The latter is easy to use for free of meteorological parameters, and its accuracy is as high as the physics-based approach. Therefore, we adopt the exponential method in this study. Previous height correction models do not consider temporal variations in height correction coefficients, which limits the correction accuracy. Hence, we consider the temporal variations in the lapse rates. The exponential method is expressed as follows:

$$ZHD = ZHD_0 \cdot e^{\frac{h-h_0}{h_d}} \quad (6)$$

$$ZWD = ZWD_0 \cdot e^{\frac{h-h_0}{h_w}} \quad (7)$$

where ZHD_0 and ZWD_0 are the zenith hydrostatic delay (m) and zenith wet delay (m) at the reference height h_0 (km), that is, the height of the grid point, h , is the target height (km). The validity range of the $h-h_0$ is the whole troposphere. h_d and h_w are the lapse rates (km) for ZHD and ZWD whose values should be determined beforehand.

As for T_m , we adopt the linear correction method (Yao et al., 2018; Zhang et al., 2017):

$$T_m = T_{m0} - \beta(h-h_0) \quad (8)$$

where T_{m0} is the weighted mean temperature (K) at h_0 (km) and β is the lapse rate (K/km).

We use the ERA5 pressure level data to calculate ZHD, ZWD, and T_m at different heights, which are then used to invert for h_d , h_w , and β by a least squares method. We find that h_d , h_w , and β show weak diurnal variations but have strong seasonal variations. We therefore neglect the diurnal variations and calculate the daily mean of these lapse rates from 2011 to 2017. We show an example in Figure 3 to demonstrate that h_d , h_w , and β have strong seasonal variations. Based on these results, we use a four-term Fourier series with annual and semiannual periods to describe their seasonal variations. Figure 3 shows that the Fourier series fit well with the h_d , h_w , and β

3.3. Establishing a New Model

The temporal variations of ZHD, ZWD, and T_m are characterized by annual, semiannual, diurnal, and semi-diurnal variations. The vertical variations of ZHD and ZWD are described by exponential functions, while the vertical variation of T_m is described by a linear model. The temporal variations in their lapse rates are

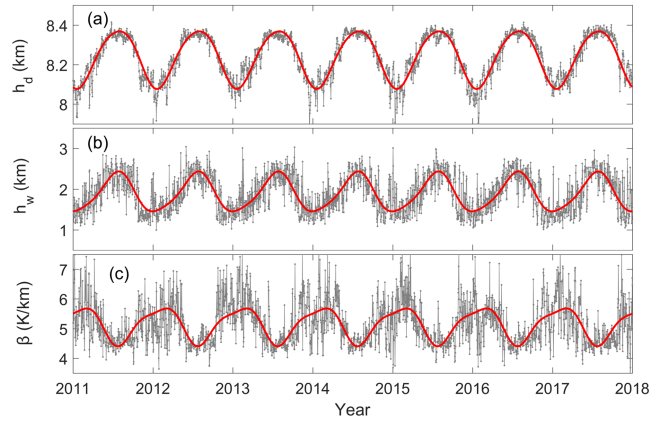


Figure 3. Time series of (a) h_d , (b) h_w , and (c) β from 2011 to 2017 at 25°N and 100°E. Red curves are the four-term Fourier series fitted to the h_d , h_w , and β .

characterized by annual and semiannual variations. We do not model the diurnal variations of lapse rates because their high-frequency variations are very weak. Considering modeling the high-frequency variations only contributes to a tiny improvement but largely increases the number of coefficients, we only model the seasonal variations. Based on these assumptions, we propose to use equations (9)–(11) to model the ZHD, ZWD, and T_m at a given point:

$$TD = \left[A_0 + A_1 \cos\left(\frac{HOD}{24} 2\pi\right) + A_2 \sin\left(\frac{HOD}{24} 2\pi\right) + A_3 \cos\left(\frac{HOD}{24} 4\pi\right) + A_4 \sin\left(\frac{HOD}{24} 4\pi\right) \right] \cdot e^{-\frac{h-h_0}{A_5}} \quad (9)$$

$$T_m = B_0 + B_1 \cos\left(\frac{HOD}{24} 2\pi\right) + B_2 \sin\left(\frac{HOD}{24} 2\pi\right) + B_3 \cos\left(\frac{HOD}{24} 4\pi\right) + B_4 \sin\left(\frac{HOD}{24} 4\pi\right) - B_5(h-h_0) \quad (10)$$

$$\begin{cases} A_i = a_{i0} + a_{i1} \cos\left(\frac{DOY}{365.25} 2\pi\right) + a_{i2} \sin\left(\frac{DOY}{365.25} 2\pi\right) + a_{i3} \cos\left(\frac{DOY}{365.25} 4\pi\right) + a_{i4} \sin\left(\frac{DOY}{365.25} 4\pi\right) \\ B_i = b_{i0} + b_{i1} \cos\left(\frac{DOY}{365.25} 2\pi\right) + b_{i2} \sin\left(\frac{DOY}{365.25} 2\pi\right) + b_{i3} \cos\left(\frac{DOY}{365.25} 4\pi\right) + b_{i4} \sin\left(\frac{DOY}{365.25} 4\pi\right) \end{cases}, \quad i = 0, 1, 2, 3, 4, 5 \quad (11)$$

where TD indicates the tropospheric delay (ZHD or ZWD), A_i and B_i ($i = 0, 1, 2, 3, 4$) are coefficients for daily variations of tropospheric delay and T_m , respectively, and A_5 and B_5 are lapse rates for tropospheric delay and T_m . All these parameters are calculated by equation (11). a_{ij} and b_{ij} ($i = 0, 1, 2, 3, 4, 5$ and $j = 0, 1, 2, 3, 4$) in equation (11) are the model coefficients to be determined.

We calculate the model coefficients at $0.5^\circ \times 0.5^\circ$ grids to account for the spatial variations. The heights of the grid points are determined by the U.S. Geological Survey/National Aeronautics and Space Administration Shuttle Radar Topography Mission Digital Elevation Model (USGS/NASA SR T_m DEM) data version 4.1 (Jarvis et al., 2008; Reuter et al., 2007). When determining the model coefficients at a given grid point, we first determine the lapse rates using the ERA5 pressure level data. Then we substitute equation (11) into equations (9) and (10) and then use the computed ZHD, ZWD, and T_m from 2011 to 2017 to invert for the model coefficients by a least squares method. We finally determine the model coefficients at all the grid points within 15–55°N and 70–135°E, which covers the whole China. This new model is named as CTrop (Chinese Tropospheric Model). Annual means and the amplitudes of annual, semiannual, diurnal, and semi-diurnal variations of ZHD, ZWD, and T_m are shown in Figure S1 of the supporting information (SI).

It should be noted that some signals (e.g., diurnals and semidiurnal variations in ZWD) may be weak in certain regions, which leads to that the corresponding coefficients are insignificant. The insignificant coefficients do not hurt the model accuracy but just introduce some redundant coefficients. Since there are so many grid points in the model, it is not wise to customize coefficients for individual ones. The CTrop model considers all the possible signals and is applicable for all points, and whether some coefficients are significant

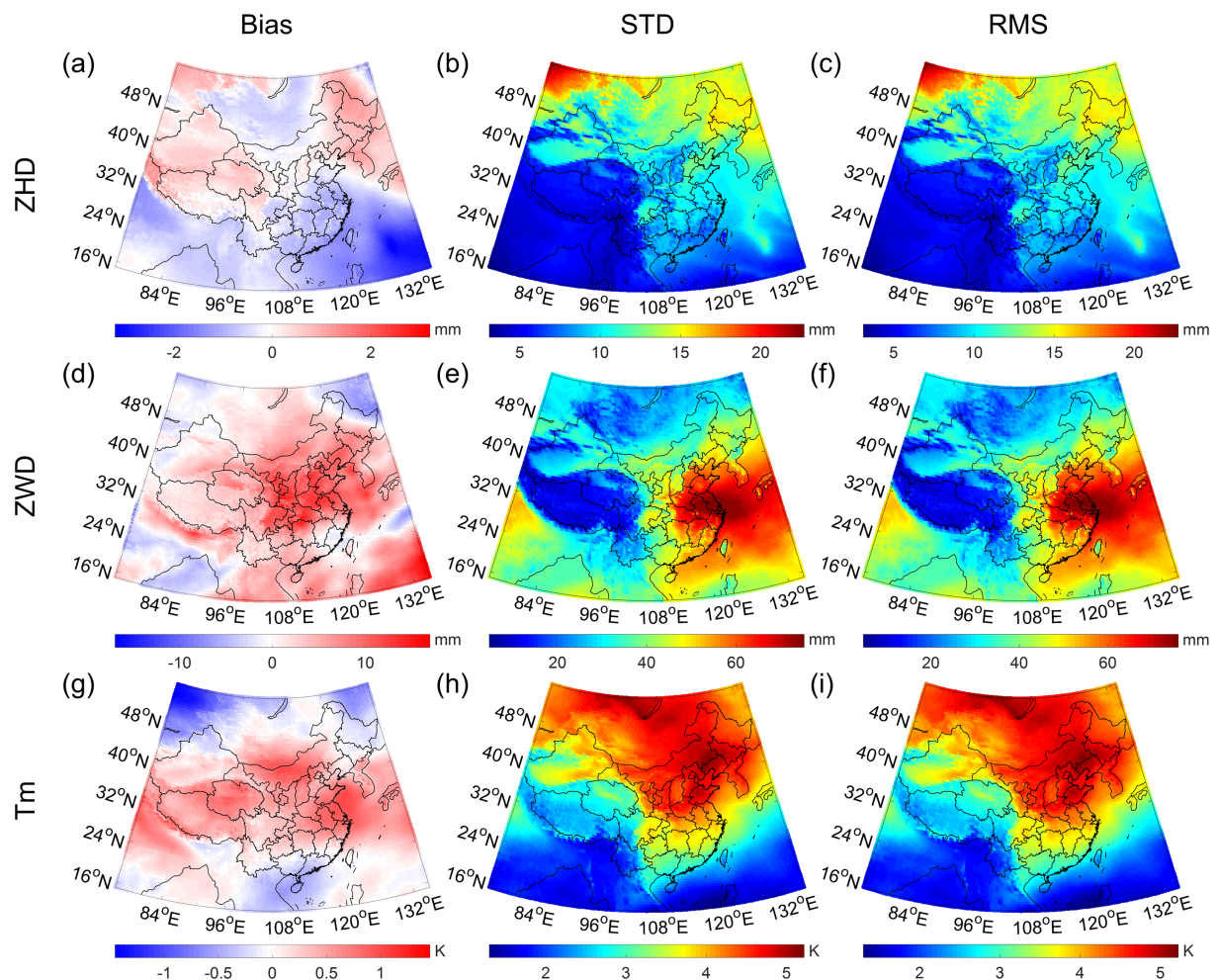


Figure 4. (a, d, g) Bias, (b, e, h) STD, and (c, f, i) RMS of ZHD, ZWD, and T_m from CTrop model validated by ERA5 hourly $0.5^\circ \times 0.5^\circ$ data in 2018. STD = standard deviation; ZHD = zenith hydrostatic delay; ZWD = zenith wet delay.

or not will not cause any difference. We calculate the WRMS for models with different coefficients numbers. The results show that the WRMS of ZHD have a reduction in the southwest of the research region when considering diurnal and semidiurnal variations (refer to Figure S2 of the SI for more information).

When using this model, only latitude, longitude, ellipsoid height, and a specific time are required. The model first finds the nearest four grid points to the given location and then calculate the required parameters at these four points at the given height through equations (9)–(11). Finally, we use a bilinear interpolation to interpolate the required parameters at the given location.

4. Results

4.1. Validate the CTrop Model by ERA5 Data

A new data set of ZHD, ZWD, and T_m retrieved from ERA5 hourly $0.5^\circ \times 0.5^\circ$ pressure level data in 2018 is employed to validate the CTrop model at heights of the grid points. For each grid point, we calculate the bias, standard deviation (STD), and root-mean-square (RMS) for ZHD, ZWD, and T_m . The results are shown in Figure 4, and the detailed statistical results are shown in Table 1.

Figure 4a shows that the ZHD has positive bias in the northwest and northeast of China and has negative bias in the southeast. The bias ranges from -3.1 to 1.4 mm with a mean value of -0.2 mm. Figure 4d shows that the ZWD has positive bias in North China. The bias ranges from -15.7 to 16.9 mm with a mean value of 2.7 mm. Figure 4g shows that the T_m has positive bias in the latitudes between 20°N and 40°N and has

Table 1
Validation Results of GPT2w, CTrop_LF, and CTrop Models Tested by ERA5 and Radiosonde Data

Validation data	Model	ZHD (mm)			ZWD (mm)			T_m (K)		
		Bias	STD	RMS	Bias	STD	RMS	Bias	STD	RMS
ERA5	GPT2w	-0.6	9.6	9.7	4.0	38.0	38.6	0.1	3.4	3.8
		[-23.0, 3.0]	[3.7, 23.2]	[3.7, 23.6]	[-87.3, 23.0]	[5.0, 75.8]	[5.9, 112.4]	[-19.4, 9.9]	[1.3, 5.3]	[1.3, 19.8]
	CTrop_LF	-0.2	9.6	9.6	2.7	37.4	37.8	0.1	3.4	3.4
		[-3.1, 1.5]	[3.7, 22.7]	[3.7, 22.7]	[-15.7, 16.9]	[4.8, 75.3]	[4.8, 75.9]	[-1.4, 1.2]	[1.3, 5.2]	[1.3, 5.2]
	CTrop	-0.2	9.3	9.4	2.7	37.3	37.7	0.1	3.3	3.4
		[-3.1, 1.5]	[3.1, 22.7]	[3.1, 22.7]	[-15.7, 16.9]	[4.7, 75.3]	[4.7, 75.9]	[-1.4, 1.2]	[1.3, 5.2]	[1.3, 5.2]
Radiosonde	GPT2w	-0.6	10.0	11.1	5.4	43.4	44.7	1.0	3.8	4.1
		[-25.3, 18.1]	[4.4, 19.2]	[5.3, 26.8]	[-19.4, 40.9]	[14.0, 77.9]	[14.0, 79.2]	[-1.9, 7.1]	[2.0, 5.6]	[2.0, 7.7]
	CTrop_LF	-0.6	10.0	11.1	3.7	43.0	43.8	-0.1	3.8	3.8
		[-22.8, 15.3]	[4.4, 19.3]	[5.2, 24.5]	[-18.5, 31.6]	[14.1, 77.2]	[14.3, 77.7]	[-1.5, 2.2]	[2.0, 5.5]	[2.0, 5.6]
	CTrop	-0.6	9.8	10.9	4.0	43.0	43.8	-0.1	3.7	3.7
		[-21.2, 16.6]	[4.0, 19.3]	[4.7, 22.9]	[-17.9, 31.9]	[14.2, 77.3]	[14.4, 77.8]	[-1.5, 2.2]	[2.0, 5.5]	[2.0, 5.6]

Note. ZHD = zenith hydrostatic delay; ZWD = zenith wet delay; STD = standard deviation; RMS = root-mean-square.

negative bias in the northwest, northeast, and south. The bias ranges from -1.4 to 1.2 K with a mean value of 0.1 K. The biases in ZHD, ZWD, and T_m are overall very small but show apparently regional characters.

The STD (Figures 4b, 4e, and 4h) and the RMS (Figures 4c, 4f, and 4i) have similar distributions, so we only describe RMS here. Figure 4c shows that the RMS of ZHD is larger in high-latitude regions and smaller in low-latitude regions, except Qinghai-Tibetan Plateau. In the Qinghai-Tibetan Plateau, the RMS of ZHD is 3.5 mm smaller in average than those in other regions, which is due to the smaller magnitudes of ZHD there than in other regions (see Figure S1a of the SI). The smaller variations in ZHD are beneficial for obtaining smaller RMS.

Figure 4f shows that the ZWD RMS is characterized by larger RMS in the east and smaller RMS in the west. In the Qinghai-Tibetan Plateau, the RMS of ZWD is 21.3 mm smaller in average than those in other regions. This is due to that the altitude of Qinghai-Tibetan Plateau is high and the climate there is dry, which leads to very small ZWD there (see Figure S1b of the SI). Small magnitudes are beneficial for obtaining small RMS. In contrast, the RMS of ZWD is apparently larger in the eastern regions than in the other regions. This is because the eastern regions are close to the west coast of Pacific Ocean and strongly influenced by the East Asian monsoon. The water vapor there is abundant and highly changeable, which causes larger RMS there (see Figures S1b, S1e, and S1h of the SI for the distribution of ZWD amplitudes).

Figure 4i shows that the RMS of T_m is apparently larger at high latitudes than those at low latitudes, except Qinghai-Tibetan Plateau. This is attributed to the stronger seasonal variations of T_m in the high-latitude regions than in low-latitude regions, which can be observed from Figures S1f and S1i of the SI. The RMS of T_m in the Qinghai-Tibetan Plateau is 0.6 K smaller in average than those in other regions, which is attributed to the small T_m amplitudes in this region (see Figure S1c of the SI).

Figure S3 of the SI shows the distributions of the RMS of the fitting residuals, which are consistent with Figures 4c, 4f, and 4i, indicating that the model accuracy is strongly correlated with the fitting accuracy.

The worst-case scenarios for ZHD, ZWD, and T_m are shown in Figure S4 of the SI. It shows that the largest ZHD RMS (22.7 mm) is located at the northwest of the research region. The largest ZWD RMS (75.9 mm) is located at the eastern region. The largest T_m RMS (5.2 K) is located at the north region. Figure S5 of the SI shows the time series of RMS of ZHD, ZWD, and T_m . It shows that the largest ZHD RMS (18.1 mm) is in winter. The largest ZWD RMS (60.2 mm) is in summer. The largest T_m RMS (5.5 K) is in winter.

4.2. Validate the CTrop Model by Radiosonde Data

ZHD, ZWD, and T_m derived from radiosonde measurements at 100 stations in 2017 are used to validate the CTrop model. Bias, STD, and RMS of ZHD, ZWD, T_m at each station are computed and presented in Figure 5.

Figures 5a, 5d, and 5g show that most of the radiosonde stations show small bias. According to our statistical results, 81% of the stations have the ZHD bias ranging from -5 to 5 mm with a mean value of 0.6 mm. Ninety

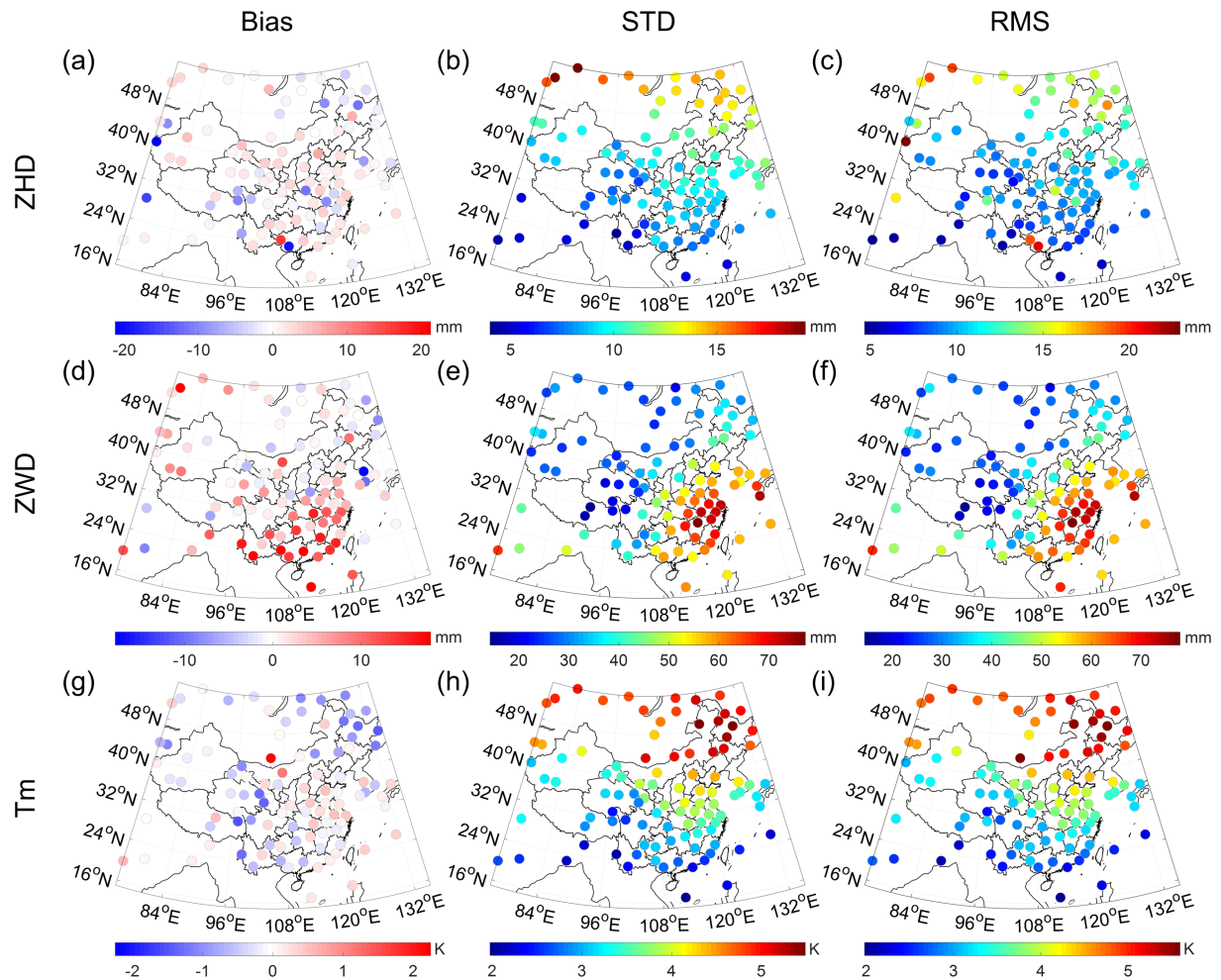


Figure 5. (a, d, g) Bias, (b, e, h) STD, and (c, f, i) RMS of ZHD, ZWD, and T_m from CTrop model validated by radiosonde data in 2017. STD = standard deviation; RMS = root-mean-square; ZHD = zenith hydrostatic delay; ZWD = zenith wet delay.

percent of the stations have the ZWD bias ranging from -15 to 15 mm with a mean value of 2.6 mm. Eighty-six percent of the stations have the bias ranging from -1 to 1 K with a mean value of -0.1 K. This indicates that the CTrop model has small bias in estimating tropospheric delay and T_m for most of the stations in the research area. The magnitudes of the mean biases are already under a low level. We attribute the biases to the difference between the ERA5 data and the radiosonde data. Detailed statistical results are shown in Table 1.

The features of STD (Figures 5b, 5e, and 5h) are similar to those of RMS (Figures 5c, 5f, and 5i), so we only discuss RMS here. Figures 5c and 5i show that the RMS of ZHD and T_m have an apparently latitudinal gradient, that is, larger at high latitudes than at low latitudes. This should be due to that the ZHD and T_m at high-latitude regions have stronger seasonal variations than at low-latitude regions. Figure 5f shows that the RMS of ZWD is larger in the southeastern region of the research area than in other regions, which is consistent with the results shown in Figure 4f.

4.3. Compare the CTrop Model With the GPT2w Model

In this section, we compare the CTrop model with the canonical GPT2w model in retrieving ZHD, ZWD, and T_m . To identify the improvement caused by introducing the diurnal and semidiurnal variations, we also compare the CTrop model with and without diurnal and semidiurnal variations. The CTrop model with only annual and semiannual signals is named as CTrop_LF hereafter. Figure 6a shows the hourly ZHD, ZWD, and T_m derived from the ERA5 data, the CTrop model, the CTrop_LF model, and the GPT2w model on DOYs 1–273, 2018 at grid point 20°N and 100°E . Figure 6b illustrates the 1-week data of Figure 6a.

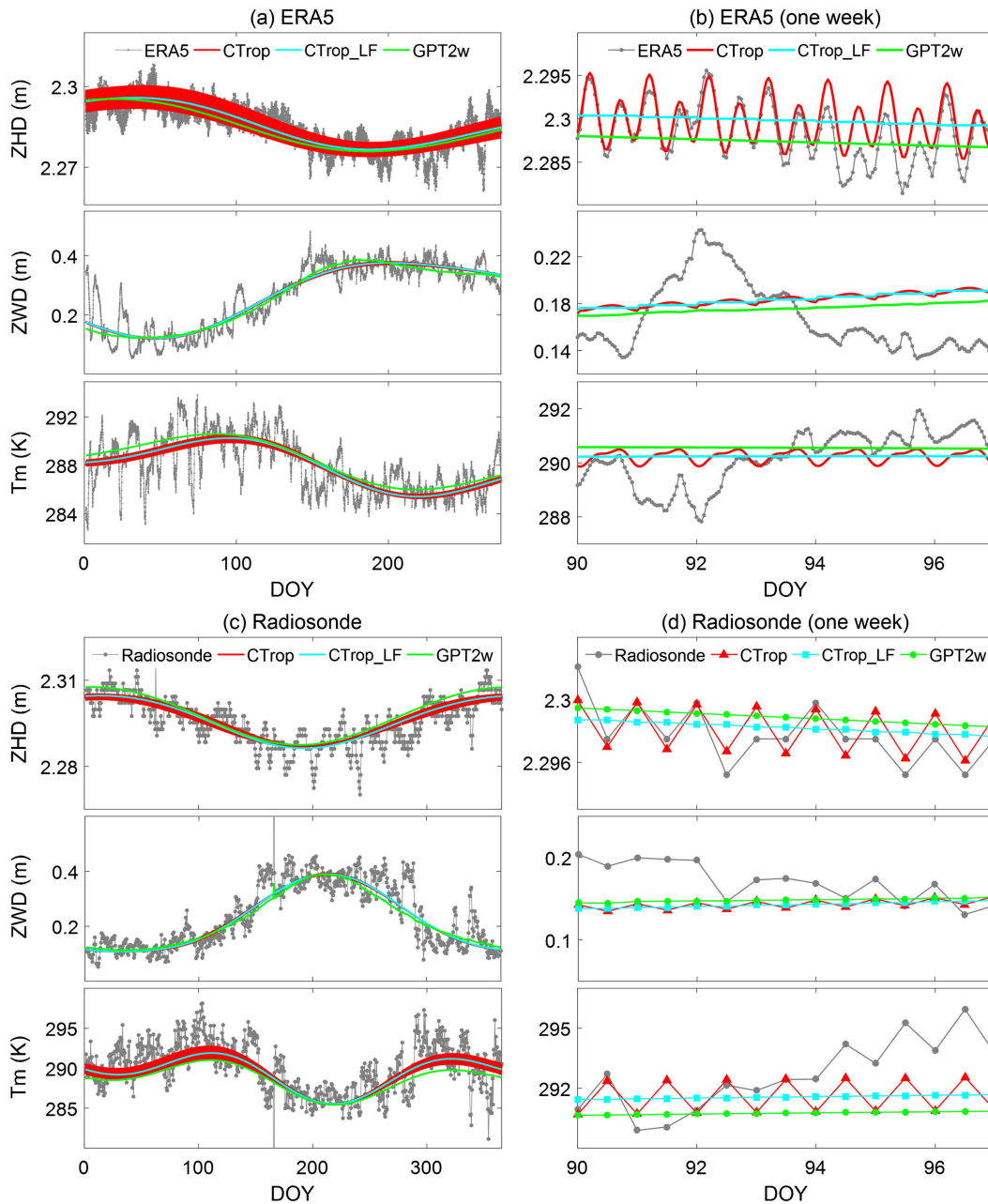


Figure 6. (a) Hourly ZHD, ZWD, and T_m derived from ERA5 data, CTrop, CTrop_LF, and GPT2w models on DOYs 1–273, 2018 at grid point 20°N and 100°E. (b) The 1-week data of Figure 6a. (c) ZHD, ZWD, and T_m derived from radiosonde data, CTrop, CTrop_LF, and GPT2w models in the whole 2017 at station INM00043003 (19.11°N and 72.85°E, in Bombay). (d) The 1-week data of Figure 6c. ZHD = zenith hydrostatic delay; ZWD = zenith wet delay; DOY = day of year.

Figure 6c shows the ZHD, ZWD and T_m derived from the radiosonde data, the CTrop model, the CTrop_LF model, and the GPT2w model in the whole 2017 at station INM00043003 (19.11°N and 72.85°E, in Bombay). Figure 6d illustrates the 1-week data of Figure 6c.

Figures 6a and 6c show that the ZHD and T_m from the CTrop model have strong seasonal variations accompanied with daily variations, and both agree well with the ERA5 and radiosonde data. The ZWD from the

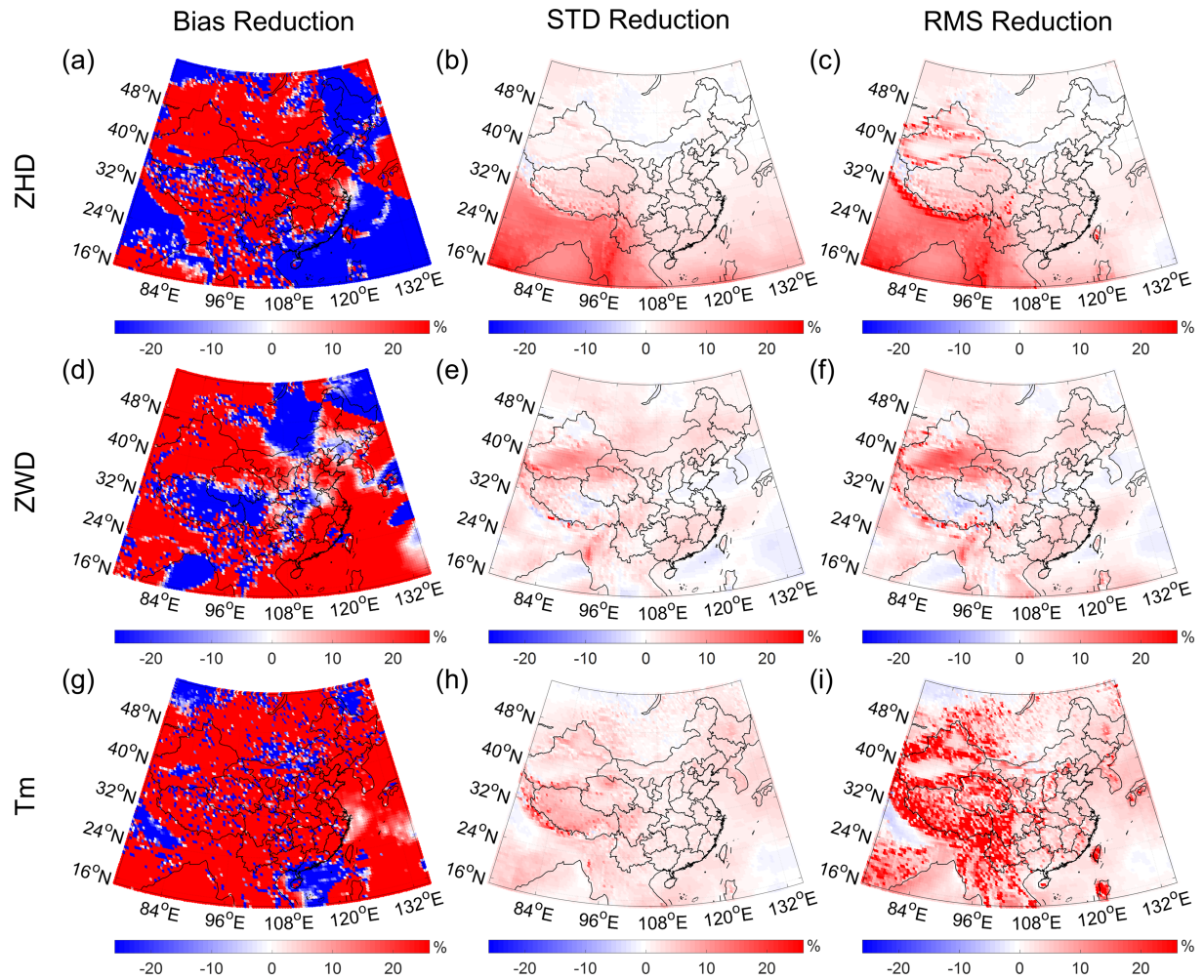


Figure 7. (a, d, g) Bias, (b, e, h) STD, and (c, f, i) RMS reductions of CTrop model compared with GPT2w model for ZHD, ZWD, and T_m validated by ERA5 data in 2018. STD = standard deviation; RMS = root-mean-square; ZHD = zenith hydrostatic delay; ZWD = zenith wet delay.

CTrop model has strong seasonal variations and weak diurnal variations and also agrees well with the ERA5 and radiosonde data. All these indicate that the CTrop model well characterizes the temporal variations of ZHD, ZWD, and T_m .

However, the GPT2w outputs and the CTrop_LF outputs are visually different from the CTrop outputs in Figures 6a and 6c. This is because the CTrop outputs show high-frequency variations, while the GPT2w outputs and the CTrop_LF outputs do not, which is evident in Figures 6b and 6d. The high-frequency variations are the diurnal and semidiurnal variations modeled by the CTrop model. Because of this, the CTrop model agrees better with the ERA5 and radiosonde data than the GPT2w and CTrop_LF models.

We demonstrate detailed statistical results validated by ERA5 and radiosonde data in Table 1. Overall, the RMS of the CTrop model is smaller than those of the GPT2w model. Validated by the ERA5 data, the RMS reductions in ZHD, ZWD, and T_m are 3.1%, 2.3%, and 10.5%, respectively. Validated by the radiosonde data, the RMS reductions become 1.8%, 2.0%, and 9.8%, respectively. This suggests that the CTrop model has better accuracies than the GPT2w model in all parameters.

The RMS of the CTrop model is slightly smaller than those of the CTrop_LF model. This indicates that considering diurnal variations leads to a slight improvement of the model performance. The RMS reductions of the CTrop(LF) models compared with the GPT2w model are larger. The CTrop(LF) models are built with the ERA5 data, and the GPT2w model is built with the ERA-Interim data. This indicates that the improvement of the model performance is largely due to the use of the new data.

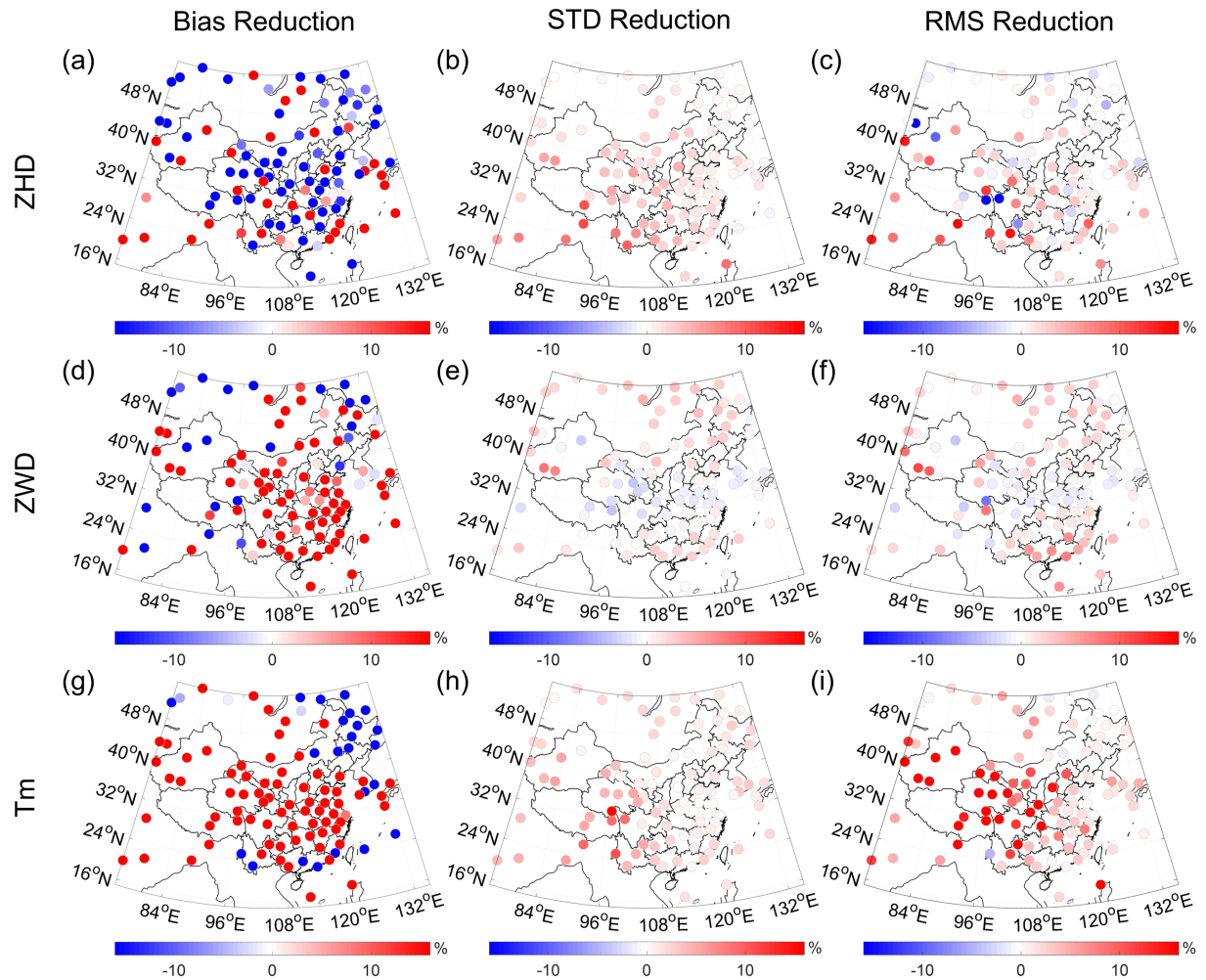


Figure 8. (a, d, g) Bias, (b, e, h) STD, and (c, f, i) RMS reductions of CTrop model compared with GPT2w model for ZHD, ZWD, and T_m validated by radiosonde data in 2017. STD = standard deviation; RMS = root-mean-square; ZHD = zenith hydrostatic delay; ZWD = zenith wet delay.

The RMS reductions of the CTrop model compared with the GPT2w model are even greater when we look at some areas. Figure 7 shows the bias, STD, and RMS reductions for ZHD, ZWD, and T_m in the whole research area. Figures 7c, 7f, and 7i show that in the western region of the research area, the RMS reductions reach 25% at some places. The distributions of these reductions are consistent with the distributions of the diurnal and semidiurnal amplitudes (see Figures S1j–S1o of the SI). This demonstrates that considering the diurnal and semidiurnal variations in modeling ZHD, ZWD, and T_m improves the model performances.

The bias, STD, and RMS reductions at each radiosonde station are computed and shown in Figure 8. Figures 8c and 8i show that the RMS reductions of ZHD and T_m are larger in the western region than in other regions. This is consistent with Figure 7, which further indicates that the CTrop model attains higher accuracy than the GPT2w model, especially in the western region.

4.4. Temporal Variations of the Model Accuracy

To investigate the temporal variations of the model accuracy, we calculate daily bias, STD, and RMS of ZHD, ZWD, and T_m from the GPT2w, the CTrop_LF, and the CTrop models validated by the radiosonde data in 2017 and shown in Figure 9.

Figure 9c shows that the RMS of ZHD from these three models is smaller in summer and larger in winter. This is because the seasonal amplitudes of ZHD are larger in winter and smaller in summer in this research area. The larger amplitudes bring more difficulties in modeling ZHD and result in larger RMS. Figure 9f

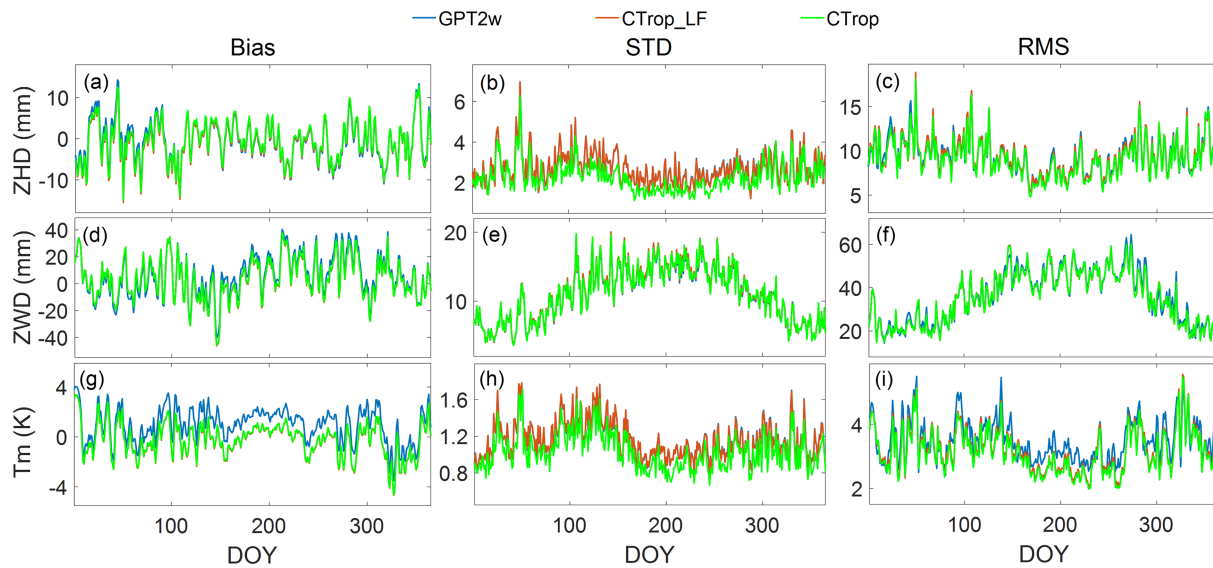


Figure 9. (a, d, g) Daily bias, (b, e, h) STD, and (c, f, i) RMS of ZHD, ZWD, and T_m from CTrop, CTrop_LF, and GPT2w models validated by radiosonde data in 2017. STD = standard deviation; RMS = root-mean-square; ZHD = zenith hydrostatic delay; ZWD = zenith wet delay.

shows that these three models both have larger RMS in estimating ZWD in summer than in winter. This should be due to that winter is drier than summer, leading to smaller ZWD in this season. The smaller ZWD is beneficial for obtaining smaller RMS. Figure 9i shows that the RMS of T_m in summer is smaller than those in winter. This is attributed to the stronger variations of T_m in winter than in summer. The stronger variations cause larger RMS.

Figures 9b and 9h show that the STD of ZHD and T_m from the CTrop_LF and the GPT2w models are similar and are apparently larger than those from the CTrop model. This STD reduction should be attributed to the high-frequency variations modeled by the CTrop model. This demonstrates that the CTrop model outperforms the GPT2w model by well capturing the diurnal and semidiurnal variations.

Figure 9g shows that the bias of T_m from the CTrop(LF) models is similar and is smaller than that from the GPT2w model. According to Table 1, the mean bias is 1.0 K for the GPT2w model and -0.1 K for the CTrop

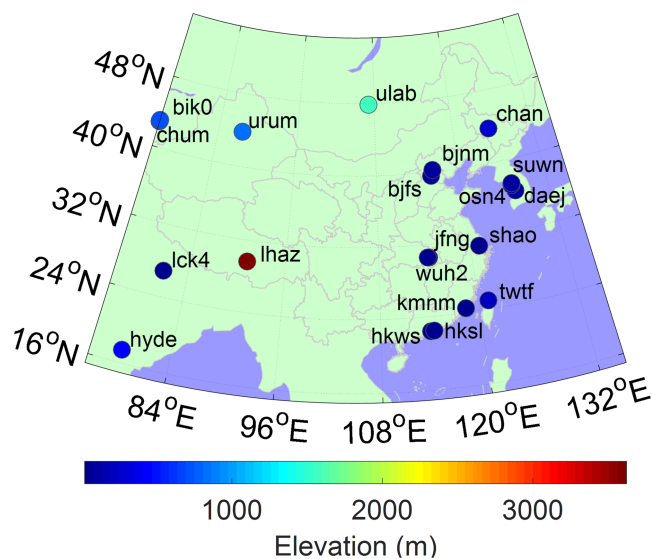


Figure 10. Distribution of selected International GNSS Service stations.

Table 2
Validation Results of GPT2w, CTrop_LF, and CTrop Models Tested by IGS ZTD

Model	Bias of ZTD (mm)	STD of ZTD (mm)	RMS of ZTD (mm)
GPT2w	1.7	47.1	48.8
	[−26.2, 17.4]	[19.1, 68.1]	[22.2, 68.8]
CTrop_LF	−0.3	46.6	47.9
	[−30.0, 14.1]	[19.7, 67.8]	[21.5, 68.0]
CTrop	−0.3	46.5	47.8
	[−30.0, 14.1]	[19.4, 67.7]	[21.2, 68.0]

Note. IGS = International GNSS Service; ZTD = zenith total delay; STD = standard deviation.

(_LF) models. This indicates that the CTrop model has better bias than the GPT2w model in computing T_m . Since the CTrop_LF model also shows better T_m bias than the GPT2w model, we attribute this improvement to our careful model of the height correction for T_m while the GPT2w model neglects this.

4.5. Validate the Model by GNSS Data

In this section, we use GNSS-derived ZTD to validate the GPT2w, CTrop_LF, and CTrop models. We collect ZTD data from 20 IGS stations in 2018 in or near China and show their distribution in Figure 10. The collected ZTD data have a temporal resolution of 5 min.

For each station, we calculate the bias, STD, and RMS of ZTD from the GPT2w, CTrop_LF, and CTrop models validated by the IGS ZTD. The statistical results are shown in Table 2. It shows that the RMS of ZTD from the CTrop model is slightly smaller than that from the GPT2w model. The RMS reduction is 2.1%. This indicates that the ZTD estimates provided by the CTrop model show higher accuracy than those from the GPT2w model. The biases of ZTD from the CTrop(_LF) models are better than that from the GPT2w model. We infer that this is because the ERA5 data have a better bias than the ERA-Interim data when compared with the IGS ZTD.

5. Discussions and Conclusions

To investigate the spectral characteristics of the model residuals, we first compute the model residuals by removing the model values output by CTrop or GPT2w from the ERA5 data and then apply FFT analysis on the residuals. Before applying FFT, we use a high-pass filter to eliminate the low-frequency signals with a threshold set to 30 days, and the exemplary power spectrums within 30 days are shown in Figure 11. This example is derived from ERA5 data and model data on DOYs 1–273, 2018 at grid point 25°N and 95°E. We

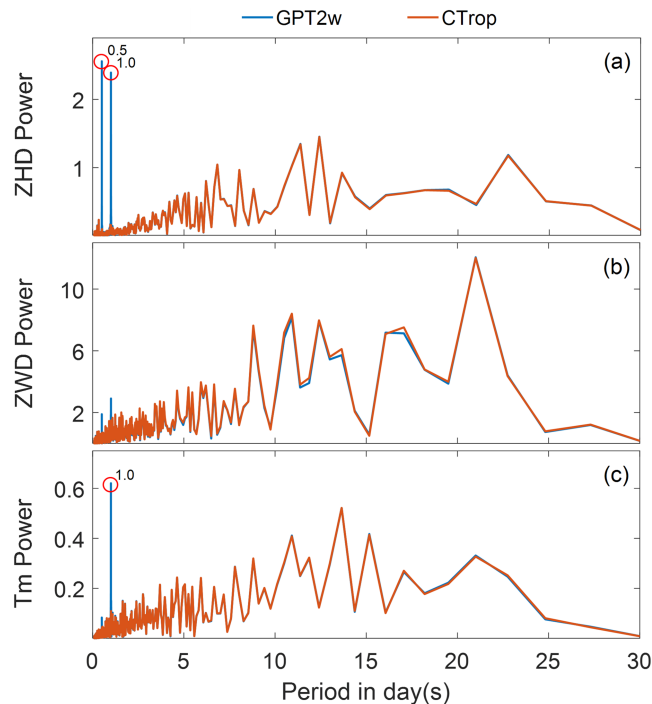


Figure 11. Power spectrums of (a) ZHD, (b) ZWD, and (c) T_m residuals from GPT2w and CTrop models. Data for this example are from ERA5 validation residuals during days of year 1–273, 2018 at grid point 25°N and 95°E. ZHD = zenith hydrostatic delay; ZWD = zenith wet delay.

select this grid point because it is a typical point that shows strong diurnal variations. It should be noted that not all the grid points simultaneously have strong diurnal variations in ZHD, ZWD, and T_m .

The power spectrum of the ZHD residuals from the GPT2w model (Figure 11a) shows two strong peaks at 0.5 and 1 day, while the power spectrum of the CTrop ZHD residuals does not show peaks at these two days. This indicates that the ZHD residuals of the GPT2w model have semidiurnal and diurnal variations, while those of the CTrop model do not. This means that we effectively model and remove the diurnal and semidiurnal variations. The power spectrum of the T_m residuals from the GPT2w model (Figure 11c) shows a strong peak at 1 day, but such a peak at 1 day does not appear in the power spectrum of the CTrop T_m residuals. This indicates that the T_m residuals of the GPT2w model have diurnal variations, while those of the CTrop model do not. These results explain the STD reductions in ZHD and T_m of the CTrop model (see Figure 9) and also further demonstrate that the CTrop model well simulate the diurnal variations of ZHD and T_m .

The power spectrums of the ZWD residuals from the GPT2w model and the CTrop model (Figure 11b) do not show a strong peak at 1 or 0.5 day; instead, they both show some unclear peaks. This should be due to the complicated variation of water vapor, which limits the modeling of ZWD.

Figures 11a–11c show that there are still many peaks in the power spectrums of the CTrop model residuals. Most of these peaks have unclear meanings and are irregular, making the residual temporal variations hard to model. These unclear variations bring uncertainties in tropospheric delay and T_m estimations and thus decrease the model performance. Therefore, how to identify and model these unclear temporal variations becomes the major problem in further improving the model accuracy, which will be left for a future study.

In this work, we use ECMWF ERA5 hourly data to investigate the temporal variations of ZHD, ZWD, and T_m . Besides the canonical seasonal variations, we confirmed that ZHD has strong diurnal and semidiurnal variations, that T_m has strong diurnal variations, and that ZWD has no clear diurnal variations. Based on their spectral characteristics, we build a new model that considers the seasonal and diurnal variations in ZHD, ZWD, and T_m , and seasonal variations in their lapse rates. This new model has the spatial resolution of $0.5^\circ \times 0.5^\circ$. Compared with the GPT2w model, the RMS reductions of this new model are 3.1%, 2.3%, and 10.5% for ZHD, ZWD, and T_m when validated by the ERA5 data. The RMS reductions become 1.8%, 2.0%, and 9.8% when validated by the radiosonde data. The reductions are greater in the western region by showing RMS reductions above 25% at some areas. When validated by the IGS ZTD, the RMS reduction of ZTD from this new model is 2.1% compared with the GPT2w model.

This new model integrates tropospheric delay and T_m modeling and thus enables GNSS receivers to measure PWV directly and is also beneficial for GNSS positioning. This new model will potentially contribute to time-critical geodetic and meteorological applications. The MATLAB source code of this new model is available online (<https://github.com/sun1753814280/CTrop>).

Acknowledgments

The authors would like to thank the European Centre for Medium-Range Weather Forecasts (ECMWF) for providing ERA5 reanalysis data, the Integrated Global Radiosonde Archive (IGRA) for providing radiosonde data, and the International GNSS Service (IGS) for providing ZTD data. The ECMWF ERA5 reanalysis data can be downloaded for free at the Climate Data Store (<https://cds.climate.copernicus.eu/cdsapp#!/dataset/reanalysis-era5-pressure-levels?tab=form>). The IGRA radiosonde data are available online (<http://www1.ncdc.noaa.gov/pub/data/igra/>). The IGS ZTD data are available online (<ftp://cdtis.gsfc.nasa.gov/gps/products/troposphere/zpd/>). Thanks also go to the GPT2w program provided by TU Vienna. The coefficients grid file and the programs are available online (<http://ggosatm.hg.tuwien.ac.at/DELAY/SOURCE/GPT2w/>). This work is supported by the National Natural Science Foundation of China (41704004 and 41574028).

References

- Albergel, C., Dutra, E., Munier, S., Calvet, J. C., Muñoz-Sabater, J., de Rosnay, P., & Balsamo, G. (2018). ERA5 and ERA-Interim driven ISBA land surface model simulations: Which one performs better? *Hydrology and Earth System Sciences*, 22(6), 3515–3532. <https://doi.org/10.5194/hess-22-3515-2018>
- Askne, J., & Nordius, H. (1987). Estimation of tropospheric delay for microwaves from surface weather data. *Radio Science*, 22(3), 379–386.
- Balidakis, K., Nilsson, T., Zus, F., Glaser, S., Heinkelmann, R., Deng, Z., & Schuh, H. (2018). Estimating integrated water vapor trends from VLBI, GPS, and numerical weather models: Sensitivity to tropospheric parameterization. *Journal of Geophysical Research: Atmospheres*, 123, 6356–6372. <https://doi.org/10.1029/2017JD028049>
- Bevis, M., Businger, S., Chiswell, S., Herring, T. A., Anthes, R. A., Rocken, C., & Ware, R. H. (1994). GPS meteorology: Mapping zenith wet delays onto precipitable water. *Journal of Applied Meteorology*, 33(3), 379–386.
- Bevis, M., Businger, S., Herring, T. A., Rocken, C., Anthes, R. A., & Ware, R. H. (1992). GPS meteorology: Remote sensing of atmospheric water vapor using the Global Positioning System. *Journal of Geophysical Research*, 97(D14), 15,787–15,801.
- Böhm, J., Heinkelmann, R., & Schuh, H. (2007). Short note: a global model of pressure and temperature for geodetic applications. *Journal of Geodesy*, 81(10), 679–683.
- Böhm, J., Möller, G., Schindelegger, M., Pain, G., & Weber, R. (2015). Development of an improved empirical model for slant delays in the troposphere (GPT2w). *GPS Solutions*, 19(3), 433–441.
- Chen, P., Yao, W., & Zhu, X. (2014). Realization of global empirical model for mapping zenith wet delays onto precipitable water using NCEP re-analysis data. *Geophysical Journal International*, 198(3), 1748–1757.
- Collins, J. P., & Langley, R. (1998). The residual tropospheric propagation delay: How bad can it get? In *Proceedings of ion GPS* (Vol. 11, pp. 729–738). Nashville, Tennessee: Institute of Navigation.
- Collins, J. P., & Langley, R. B. (1997). *A tropospheric delay model for the user of the wide area augmentation system*. Fredericton: Department of Geodesy and Geomatics Engineering, University of New Brunswick.

- Davis, J. L., Herring, T. A., Shapiro, I. I., Rogers, A. E. E., & Elgered, G. (1985). Geodesy by radio interferometry: Effects of atmospheric modeling errors on estimates of baseline length. *Radio Science*, 20(6), 1593–1607.
- Ding, M. (2018). A neural network model for predicting weighted mean temperature. *Journal of Geodesy*, 1–12.
- Dodson, A. H., Chen, W., Baker, H. C., Penna, N. T., Roberts, G. W., Jeans, R. J., & Westbrook, J. (1999). Assessment of EGNOS tropospheric correction model. In ION GPS-99 (pp. 1401–1407).
- Hackman, C., & Byram, S. M. (2012). IGS troposphere working group 2013. IGS Central Bureau, 183.
- He, C., Wu, S., Wang, X., Hu, A., Wang, Q., & Zhang, K. (2017). A new voxel-based model for the determination of atmospheric weighted mean temperature in GPS atmospheric sounding. *Atmospheric Measurement Techniques*, 10(6), 2045–2060. <https://doi.org/10.5194/amt-10-2045-2017>
- Hersbach, H., & Dee, D. (2016). ERA5 reanalysis is in production. *ECMWF Newsletter*, 147(7).
- Hopfield, H. S. (1971). Tropospheric effect on electromagnetically measured range: Prediction from surface weather data. *Radio Science*, 6(3), 357–367.
- Huang, L., Jiang, W., Liu, L., Chen, H., & Ye, S. (2018). A new global grid model for the determination of atmospheric weighted mean temperature in GPS precipitable water vapor. *Journal of Geodesy*, 1–18.
- Ifadis, I. M. (1993). Space to earth techniques: Some considerations on the zenith wet path delay parameters. *Survey Review*, 32(249), 130–144.
- Jarvis, A., Reuter, H. I., Nelson, A., Guevara, E. (2008) Hole-filled seamless SRTM data V4, International Centre for Tropical Agriculture (CIAT), available from <http://srtm.csi.cgiar.org>.
- Krueger, E., Schueler, T., & Arbesser-Rastburg, B. (2005). The standard tropospheric correction model for the European satellite navigation system Galileo. Proc. General Assembly URSI.
- Lagler, K., Schindelegger, M., Böhm, J., Krásná, H., & Nilsson, T. (2013). GPT2: Empirical slant delay model for radio space geodetic techniques. *Geophysical Research Letters*, 40, 1069–1073. <https://doi.org/10.1002/grl.50288>
- Landskron, D., & Böhm, J. (2018). VMF3/GPT3: Refined discrete and empirical troposphere mapping functions. *Journal of Geodesy*, 92(4), 349–360.
- Leick, A., Rapoport, L., & Tatarnikov, D. (2015). *GPS satellite surveying*. Hoboken, New Jersey: John Wiley & Sons.
- Li, W., Yuan, Y., Ou, J., Chai, Y., Li, Z., Liou, Y. A., & Wang, N. (2015). New versions of the BDS/GNSS zenith tropospheric delay model IGGtrop. *Journal of Geodesy*, 89(1), 73–80.
- Li, W., Yuan, Y., Ou, J., & He, Y. (2018). IGGtrop_SH and IGGtrop_rH: Two improved empirical tropospheric delay models based on vertical reduction functions. *IEEE Transactions on Geoscience and Remote Sensing*. <https://doi.org/10.1109/tgrs.2018.2812850>
- Li, W., Yuan, Y., Ou, J., Li, H., & Li, Z. (2012). A new global zenith tropospheric delay model IGGtrop for GNSS applications. *Chinese Science Bulletin*, 57(17), 2132–2139.
- Penna, N., Dodson, A., & Chen, W. (2001). Assessment of EGNOS tropospheric correction model. *The Journal of Navigation*, 54(1), 37–55.
- Reuter, H. I., Nelson, A., & Jarvis, A. (2007). An evaluation of void-filling interpolation methods for SRTM data. *International Journal of Geographical Information Science*, 21(9), 983–1008.
- Rüeger, J. M. (2002). *Refractive index formulae for radio waves, JS28 integration of techniques and corrections to achieve accurate engineering*. Washington, DC: FIG XXII International Congress.
- Saastamoinen, J. (1972). Atmospheric correction for the troposphere and stratosphere in radio ranging satellites. In S. W. Henriksen, A. Mancini, & B. H. Chovitz (Eds.), *The Use of Artificial Satellites for Geodesy, Geophysics Monograph Series* (Vol. 15, pp. 247–251). Washington, DC: American Geophysical Union.
- Schüler, T. (2014). The TropGrid2 standard tropospheric correction model. *GPS Solutions*, 18(1), 123–131.
- Tregoning, P., & Herring, T. A. (2006). Impact of a priori zenith hydrostatic delay errors on GPS estimates of station heights and zenith total delays. *Geophysical Research Letters*, 33, L23303. <https://doi.org/10.1029/2006GL027706>
- Wang, X., Zhang, K., Wu, S., Fan, S., & Cheng, Y. (2016). Water vapor-weighted mean temperature and its impact on the determination of precipitable water vapor and its linear trend. *Journal of Geophysical Research: Atmospheres*, 121, 833–852. <https://doi.org/10.1002/2015JD024181>
- Yao, Y., Hu, Y., Yu, C., Zhang, B., & Guo, J. (2016). An improved global zenith tropospheric delay model GZTD2 considering diurnal variations. *Nonlinear Processes in Geophysics*, 23(3), 127–136.
- Yao, Y., Sun, Z., Xu, C., Xu, X., & Kong, J. (2018). Extending a model for water vapor sounding by ground-based GNSS in the vertical direction. *Journal of Atmospheric and Solar-Terrestrial Physics*, 179, 358–366.
- Yao, Y., Xu, C., Shi, J., Cao, N., Zhang, B., & Yang, J. (2015). ITG: A new global GNSS tropospheric correction model. *Scientific Reports*, 5(1), 10273. <https://doi.org/10.1038/srep10273>
- Yao, Y., Xu, C., Zhang, B., & Cao, N. (2014). GTM-III: A new global empirical model for mapping zenith wet delays onto precipitable water vapour. *Geophysical Journal International*, 197(1), 202–212. <https://doi.org/10.1093/gji/ggu008>
- Yao, Y., Zhu, S., & Yue, S. (2012). A globally applicable, season-specific model for estimating the weighted mean temperature of the atmosphere. *Journal of Geodesy*, 86(12), 1125–1135.
- Yao, Y. B., Zhang, B., Yue, S. Q., Xu, C. Q., & Peng, W. F. (2013). Global empirical model for mapping zenith wet delays onto precipitable water. *Journal of Geodesy*, 87(5), 439–448.
- Zhang, H., Yuan, Y., Li, W., Ou, J., Li, Y., & Zhang, B. (2017). GPS PPP-derived precipitable water vapor retrieval based on Tm/Ps from multiple sources of meteorological data sets in China. *Journal of Geophysical Research: Atmospheres*, 122, 4165–4183. <https://doi.org/10.1002/2016JD026000>

Erratum

In the originally published version of this article, Figure 6 was incorrect. The figure has since been updated and this version may be considered the authoritative version of record.